Observation of charge to spin conversion in Weyl semimetal WTe2 at room temperature

Citation for the original published paper (version of record):
Zhao, B., Khokhriakov, D., Zhang, Y. et al (2020). Observation of charge to spin conversion in Weyl semimetal WTe2 at room temperature. Physical Review Research, 2(1).
http://dx.doi.org/10.1103/PhysRevResearch.2.013286

PHYSICAL REVIEW RESEARCH **2**, 013286 (2020)

Observation of charge to spin conversion in Weyl semimetal WTe_2 at room temperature

Bing Zhao,[1,2] Dmitrii Khokhriakov,[2] Yang Zhang,[3] Huixia Fu,[4] Bogdan Karpiak,[2] Anamul Md. Hoque,[2]
Xiaoguang Xu,[1] Yong Jiang,[1] Binghai Yan,[4] and Saroj P. Dash[2,5,*]
[1]*Beijing Advanced Innovation Center for Materials Genome Engineering, School of Materials Science and Engineering, University of Science and Technology Beijing, Beijing 100083, China*
[2]*Department of Microtechnology and Nanoscience, Chalmers University of Technology, SE-41296 Göteborg, Sweden*
[3]*Max Planck Institute for Chemical Physics of Solids, D-01187 Dresden, Germany*
[4]*Department of Condensed Matter Physics, Weizmann Institute of Science, Rehovot 7610001, Israel*
[5]*Graphene Center, Chalmers University of Technology, SE-41296 Göteborg, Sweden*

(Received 20 September 2019; accepted 29 January 2020; published 10 March 2020)

The discovery of topological Weyl semimetals has revealed opportunities to realize several extraordinary physical phenomena in condensed matter physics. Specifically, Weyl semimetals with strong spin-orbit coupling, broken inversion symmetry, and novel spin textures are predicted to exhibit a large spin Hall effect that can efficiently convert the charge current to a spin current. Here, we report a direct experimental observation of large spin Hall and inverse spin Hall effects in the Weyl semimetal WTe_2 at room temperature obeying the Onsager reciprocity relation. We demonstrate the detection of a pure spin current generated by the spin Hall phenomenon in WTe_2 by making a van der Waals heterostructure with graphene, taking advantage of its long spin coherence length and spin transmission at the heterostructure interface. These experimental findings, well supported by *ab initio* calculations, show a large charge-spin conversion efficiency in WTe_2, which can pave the way for the utilization of spin-orbit-induced phenomena in spintronic memory and logic circuit architectures.

DOI: 10.1103/PhysRevResearch.2.013286

I. INTRODUCTION

A strong resurgence of interest in two-dimensional (2D) transition metal dichalcogenides (TMDs) has been sparked with the successful preparation of materials with different properties that have the potential to revolutionize the future of electronics [1,2]. While semiconducting TMDs have caused enormous interest in transistors [3–6] and optoelectronic applications [7], semimetals are predicted to host novel topological electronic states [8–10]. The recently predicted type-II Weyl semimetals [10–12] such as WTe_2 show extraordinary electronic phenomena, such as a giant magnetoresistance [13], high mobilities [14], chiral anomaly [15], and an anomalous Hall effect [16]. These novel transport features indicate the existence of Weyl fermionic states, which are characterized by a tilted linear dispersion of Weyl cones and Fermi arc surface states. Due to the monopolelike Berry curvature in the momentum space, a strong spin-orbit interaction, a unique spin texture in Weyl cones and Fermi arc surface states are predicted to exist [17–19]. In addition to the topological Weyl features in these semimetals, trivial spin-polarized Fermi arc surface states are also shown to exist at the Fermi level between the electron and hole pockets at room temperature [20–26]. Taking advantage of these properties, recent experiments with WTe_2/ferromagnet bilayers showed a control of the spin-orbit torque arising from their crystal symmetry [27,28]. Therefore, these 2D semimetals are considered to have a huge potential for ultralow-power spintronic devices [29] with an efficient conversion of charge-to-spin current, i.e., a large spin Hall effect (SHE) and (or) Rashba-Edelstein effect (REE) at room temperature [30]; however, it has not yet been experimentally measured.

Here, we report the observation of a large spin Hall effect (SHE) and inverse spin Hall effect (ISHE) in semimetal WTe_2 devices at room temperature. We electrically detect the SHE and ISHE signals in WTe_2 by employing a van der Waals heterostructure device with a graphene channel, taking advantage of the 2D layered structures of both classes of materials. In these experiments, we exploit the best of both the worlds, such as a large spin Hall angle of WTe_2, along with a long spin coherence length in graphene [31,32] and an efficient spin transfer at the WTe_2-graphene interface. Our detailed spin-sensitive electronic measurements both in the in-plane and perpendicular geometries, angle- and gate-dependent studies, and theoretical calculations manifest the existence of large spin Hall phenomena in WTe_2 devices at room temperature.

II. RESULTS

Figures 1(a) and 1(b) show our calculated crystal structure and electronic structure, respectively, for WTe_2 in the T_d phase. At the Fermi surface, small electron and hole pockets coexist, demonstrating a compensating semimetallic feature. Because of inversion symmetry breaking and strong spin-orbit coupling (SOC), each pocket splits into two bands

---

[*] Corresponding author: saroj.dash@chalmers.se

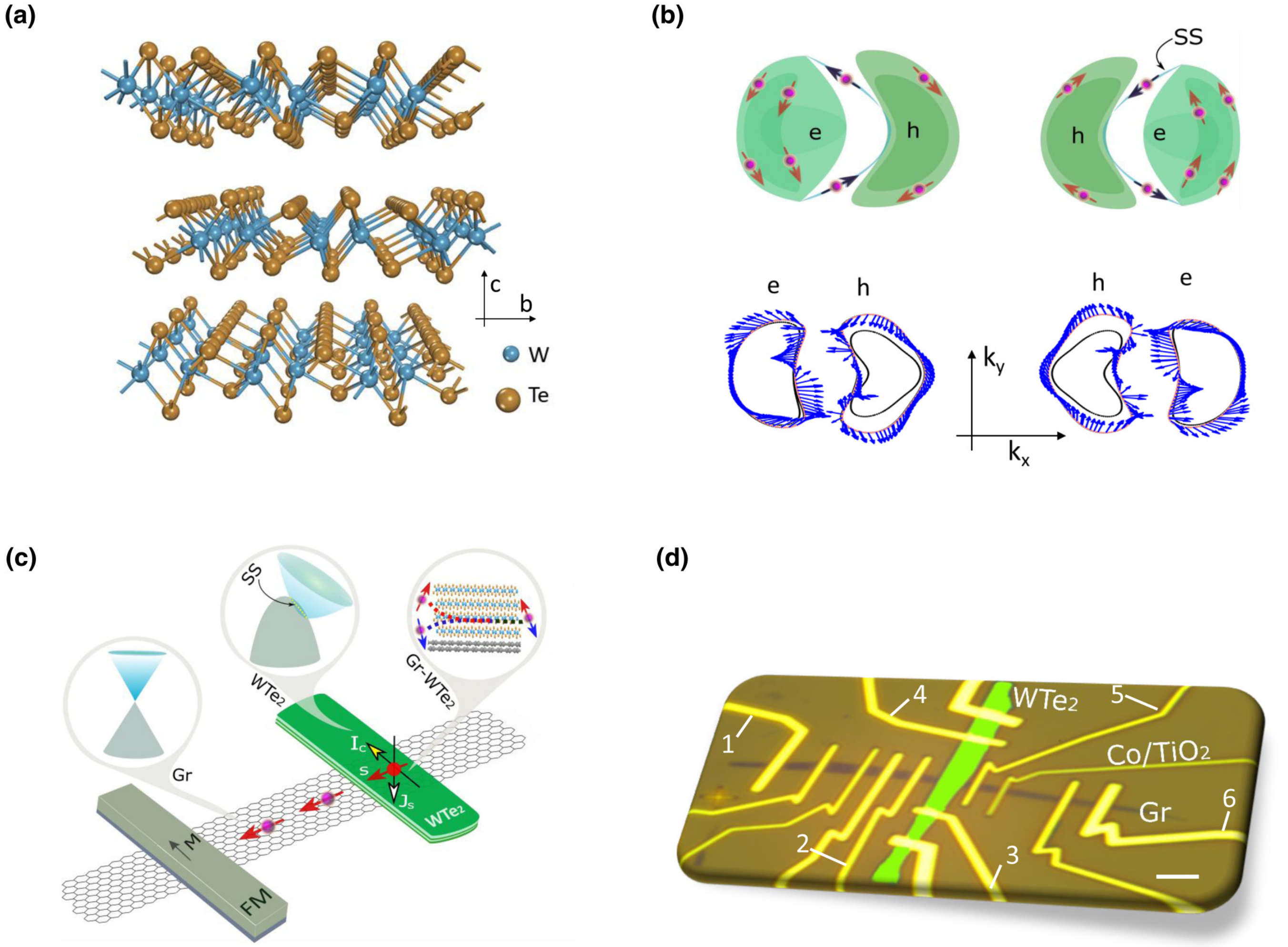

FIG. 1. Scheme for detection of the spin Hall effect and inverse spin Hall effect in WTe_2. (a) Crystal structure of the WTe_2 in T_d phase showing the layered nature. (b) Top: Schematic of the spin textures at the Fermi surface with the electron (*e*), hole (*h*) pockets, and the surface states (SS). Bottom: Our calculated electronic structure showing the coexistence of both the *e* and *h* pockets on the Fermi surface. Both the electron and hole bands split into two bands (red and black). The spin texture is indicated by blue arrows in one of the split bands (red). The two split bands have opposite directions of spin polarization. (c), (d) Schematics and a representative colored optical microscope picture of a nanofabricated WTe_2-graphene van der Waals heterostructure device with WTe_2 flake (green), ferromagnetic tunnel contacts of TiO_2/Co (FM) on the graphene (Gr) channel for the measurement of SHE, and the ISHE on a SiO_2/Si substrate. The insets in the schematics show the band structures of the materials and the structure at the interface. The scale bar (white) in the device picture is 2 μm. For SHE or ISHE measurements, for example, FM contacts nearest to WTe_2 are used for spin detection or injection with current through contacts 3,4 ($I_{3,4}$) and voltage measured via contacts 1,2 ($V_{1,2}$) and vice versa, respectively.

[see Fig. 1(b)]. The Fermi surface exhibits a clear spin texture [30,33]. The left and right parts of the Fermi surface and spin texture can be transformed into each other by a mirror reflection (k_x to $-k_x$). Such as strong spin-momentum locking feature indicates that the charge current comes together with a spin current, such as SHE and REE. We experimentally investigated the influence of the spin degree of freedom on the charge currents and vice versa due to the presence of strong SOC, broken inversion symmetry, and the novel spin textures in WTe_2. The SHE in WTe_2 is expected to cause a transverse spin current induced by a charge current, whereas the inverse SHE (ISHE) produces a transverse charge current that is caused by a pure spin current [34,35].

Figures 1(c) and 1(d) show the schematics and nanofabricated devices consisting of van der Waals heterostructures of WTe_2 with graphene. The heterostructure of graphene with WTe_2 flakes of 11–30 nm thickness was used (from Hq Graphene), as measured by an atomic force microscope (AFM) (see Fig. S1 in the Supplemental Material [36]). The quality of the WTe_2 was characterized by a Raman spectrometer, showing peaks corresponding to the T_d phase (Fig. S2 in the Supplemental Material [36]). We used both exfoliated and chemical-vapor-deposited (CVD) graphene-based devices. While the exfoliated graphene devices were prepared by the dry transfer method, the CVD graphene-WTe_2 devices were made by exfoliation of WTe_2 and the dry transfer process inside a glove box. Contacts to graphene and WTe_2 were defined by standard electron beam lithography and lift-off process. For the preparation of ferromagnetic tunnel contacts to graphene, a two-step deposition of 0.3 nm of Ti and an

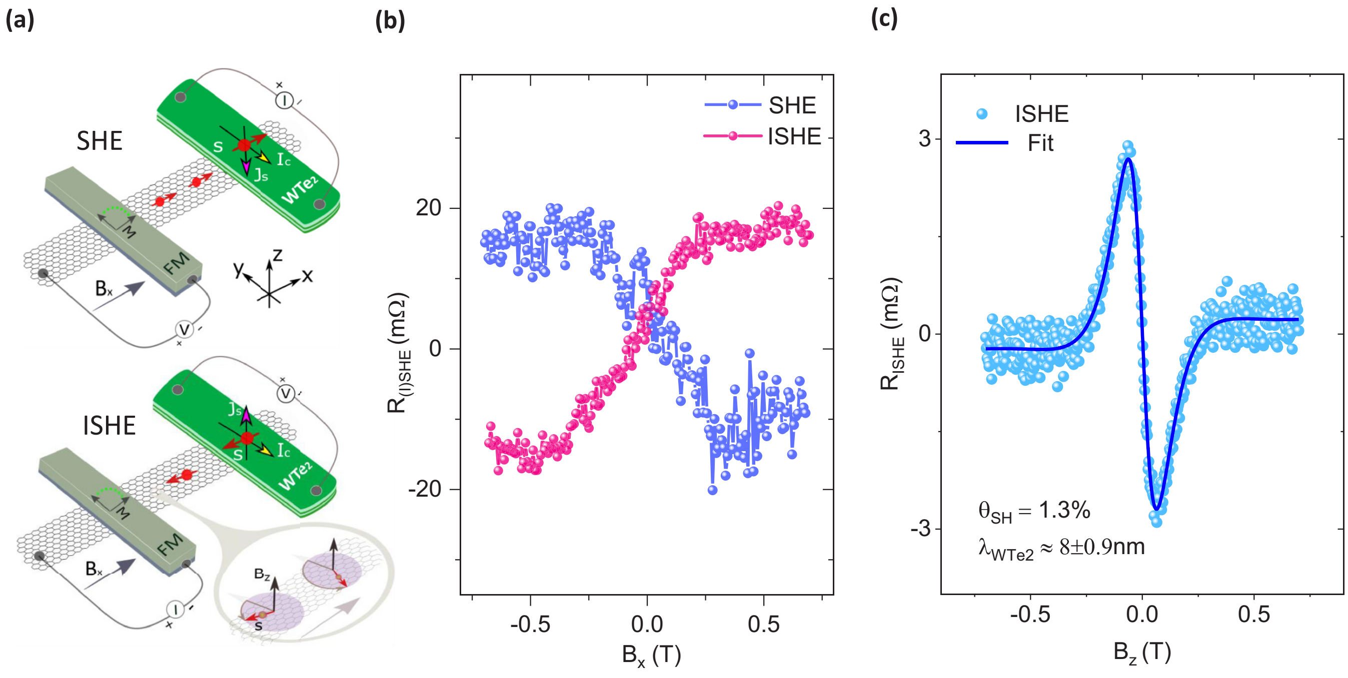

FIG. 2. Electrical detection of the spin Hall effect and inverse spin Hall effect in WTe_2 at room temperature. (a) Top: Schematic diagram of SHE measurement configuration, where a charge current in WTe_2 induces a spin current, which is injected and detected in graphene using a ferromagnetic contact in a nonlocal geometry, while the direction of the applied magnetic field sweep is B_x. Bottom: Schematic representation of ISHE measurement configuration, where a spin current injected from a ferromagnetic electrode into graphene enters the WTe_2 channel and hence induces a charge current giving rise to a voltage signal in WTe_2, while the applied magnetic field sweeps along B_x and B_z, respectively. The inset is the out-of-plane B_z-induced spin precession. (b) The change in SHE and ISHE resistance [$R_{\mathrm{(I)SHE}} = V_{\mathrm{(I)SHE}}/I$] with magnetic field B_x sweep due to the (I)SHE for bias currents of $+60\ \mu$A at room temperature for device No. 1 with channel length $L_{\mathrm{SHE}} = 2.6\ \mu$m between Co and WTe_2. (c) ISHE signal data and fitting curve with out-of-plane magnetic field B_z in device No. 3 with channel length $L_{\mathrm{SHE}} = 3.5\ \mu$m at bias currents of $+100\ \mu$A. The ISHE signal data shown here were an average of five repeated field sweep measurements. All the measurements were performed at 300 K.

oxidation process was carried out, followed by 100 nm of Co deposition. The ferromagnetic tunnel contact (TiO_2/Co) resistances on the graphene channel were in the range of a few kΩ.

Figure 2(a) show the measurement geometries for SHE and ISHE in a hybrid device consisting of a WTe_2-graphene heterostructure and a ferromagnetic contact. The contact resistance of WTe_2-graphene in device No. 1 during SHE measurements was around ∼2 kΩ μm^2 (Fig. S3a in the Supplemental Material [36]). The application of longitudinal charge current (I) in WTe_2 produces a pure transverse spin current due to SHE, which is injected into the graphene at the interface and subsequently detected as a voltage signal (V_{SHE}) by the nonlocal ferromagnetic Co tunnel contacts. The direction of the injected spins is in the plane of the graphene and perpendicular to the ferromagnet electrodes. The magnetic field B_x is applied perpendicular to the electrodes for changing the magnetization direction of Co from 90° to 0° with respect to the injected spins. Figure 2(b) shows the measured SHE data of $R_{\mathrm{SHE}} = V_{\mathrm{SHE}}/I$ for $I = 60\ \mu$A at room temperature for a B_x sweep for device No. 1 with a graphene channel length $L_{\mathrm{SHE}} = 2.6\,\mu$m. As expected, R_{SHE} follows a linear dependence at low B field, due to the $\sin(\theta)$ dependence of the ferromagnetic moment rotation angle θ with the Co electrodes, whereas at large enough B field, the magnetization of Co rotates 90° and become parallel to the B field and also the injected spin directions, resulting in the saturation of R_{SHE}. In the device fabrication, the contacts to WTe_2 are also made of Co, however, the large SOC in WTe_2 causes the injected spins from Co to dephase within a few nanometers due to the strong spin scattering. Therefore, we can rule out the contribution of spin injection from Co into WTe_2 in the SHE measurements.

Next, we performed the ISHE experiment, where a pure spin current is injected from the ferromagnet and absorbed by WTe_2. The spin current at the WTe_2-graphene interface should give rise to a transversal charge voltage (V_{ISHE}) due to the ISHE [Fig. 2(a)]. Figure 2(b) shows the measured ISHE data of $R_{\mathrm{ISHE}} = V_{\mathrm{ISHE}}/I$ for $I = 60\ \mu$A at room temperature with $\sin(\theta)$ behavior for a B_x field sweep. These observed features confirm that the measured signal arises from spin to charge conversion in WTe_2. According to our measurement geometry and the SHE signal [Figs. 2(a) and 2(b)], the spin Hall angle θ_{SH} is positive based on $I_s \propto s \times I_c$ [37]. This is confirmed by a bias current polarity dependence of the (I)SHE signals (see Fig. S5 in the Supplemental Material [36]). Both the signals R_{SHE} and R_{ISHE} saturate with the magnetization of the injector/detector ferromagnetic Co electrode, as verified from the spin precession Hanle measurements with the B_x field in the graphene channels (see Fig. S7 in the Supplemental Material [36]). The observed comparable SHE and ISHE signal magnitudes, and their line shapes with magnetic field sweeps are in agreement with the Onsager reciprocity relation

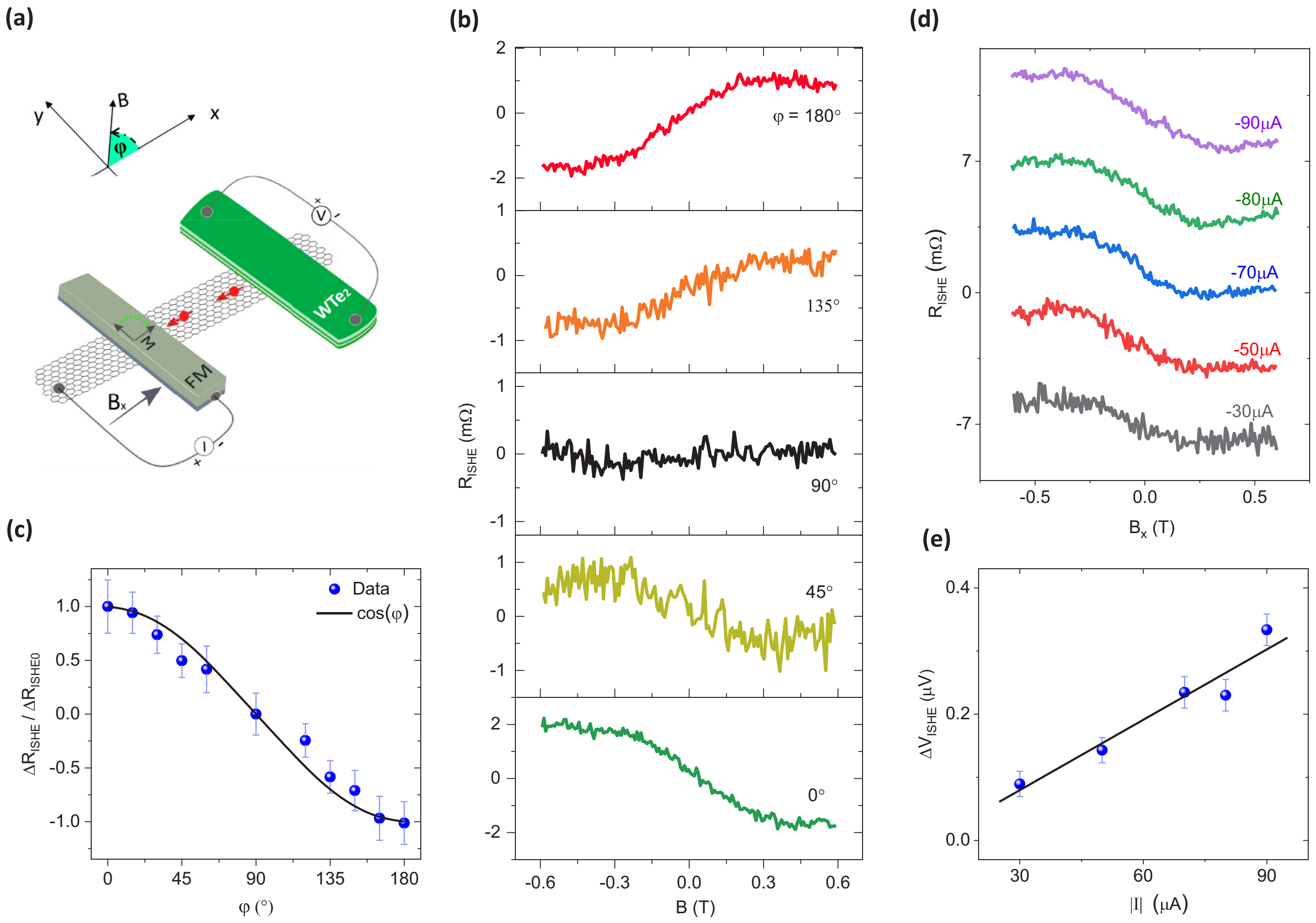

FIG. 3. Angle dependence of the inverse spin Hall effect in WTe_2. (a) Schematic representation of the ISHE measurement geometry with directions of an applied magnetic field, the detector ferromagnet magnetization, and the spin current. The angle φ is defined as shown in the inset. (b) The ISHE resistance R_{ISHE} measured at room temperature for various measurement angle orientations for device No. 2 with a graphene channel length of $L_{\mathrm{SHE}} = 3.5\ \mu\mathrm{m}$. (c) The normalized magnitude of ΔR_{ISHE} as a function of the magnetic field angle φ. The solid line is the cos(φ) curve. (d), (e) The measured R_{SHE} at different spin injection bias currents with a shift at the y axis for the sake of clarity and the magnitude of the ISHE signal with an applied bias current for device No. 2. All the measurements were performed at 300 K.

[38] and demonstrate the generation and detection of pure spin currents in WTe_2.

To further verify the charge-spin conversion, out-of-plane B_z field sweep measurements were also performed in the ISHE configuration in device No. 3. Device No. 3 consists of monolayer graphene, 11 nm WTe_2 with 1 μm width and 25 $\Omega\ \mu\mathrm{m}^2$ graphene-WTe_2 interface resistance (see Table 1 in the Supplemental Material for details about the device [36]). The spin current injected from the ferromagnetic (FM) electrode experiences a spin precession in the graphene channel ($L = 3.5\ \mu$m) as the B_z field is perpendicular to the graphene plane. Subsequently, the spin current gets absorbed ~100% at the graphene/WTe_2 interface for the monolayer graphene device used here [see Fig. S9(d) in the Supplemental Material [36]] and gives rise to a transversal charge voltage (V_{ISHE}), where $R_{\mathrm{ISHE}} = V_{\mathrm{ISHE}}/I$ [Fig. 2(c)]. Contrary to the in-plane ISHE with B_x field sweep, here the magnetization of FM does not rotate with the B_z field in this field sweep range and remains in plane. The observed R_{ISHE} is antisymmetric with the B_z field. At $B_z = 0$, the injected spins are oriented along with the WTe_2 flake without any precession and results in $R_{\mathrm{ISHE}} = 0$ as it lacks the right-hand rule for the observation of ISHE [37,39] in the measured geometry. At a finite B_z field, maximum (minimum) values of R_{ISHE} are obtained when the precession provides a spin component perpendicular to the WTe_2 long axis. Finally, at a larger B_z field, R_{ISHE} decreases with an increase in the spin precession angle and approaches zero due to complete spin dephasing [40]. The in-plane (B_x) ISHE measurements in the same device No. 3 are presented in Fig. S6 in the Supplemental Material [36]. Both the in-plane (B_x) and out-of-plane (B_z) measurements unambiguously demonstrate that the in-plane spins are responsible for the induction of the ISHE signal in WTe_2. The magnitude of the measured (I)SHE signals (up to ~30 mΩ) in WTe_2 are very large, which are two orders of magnitude larger than measured in metals (Pt) in heterostructures with Cu [41], and three times larger than Pt in heterostructures with graphene [40,42], indicating a very large spin Hall angle θ_{SH} in WTe_2. This can be confirmed by the large spin valve signal reduction since the spin absorption by WTe_2 is the

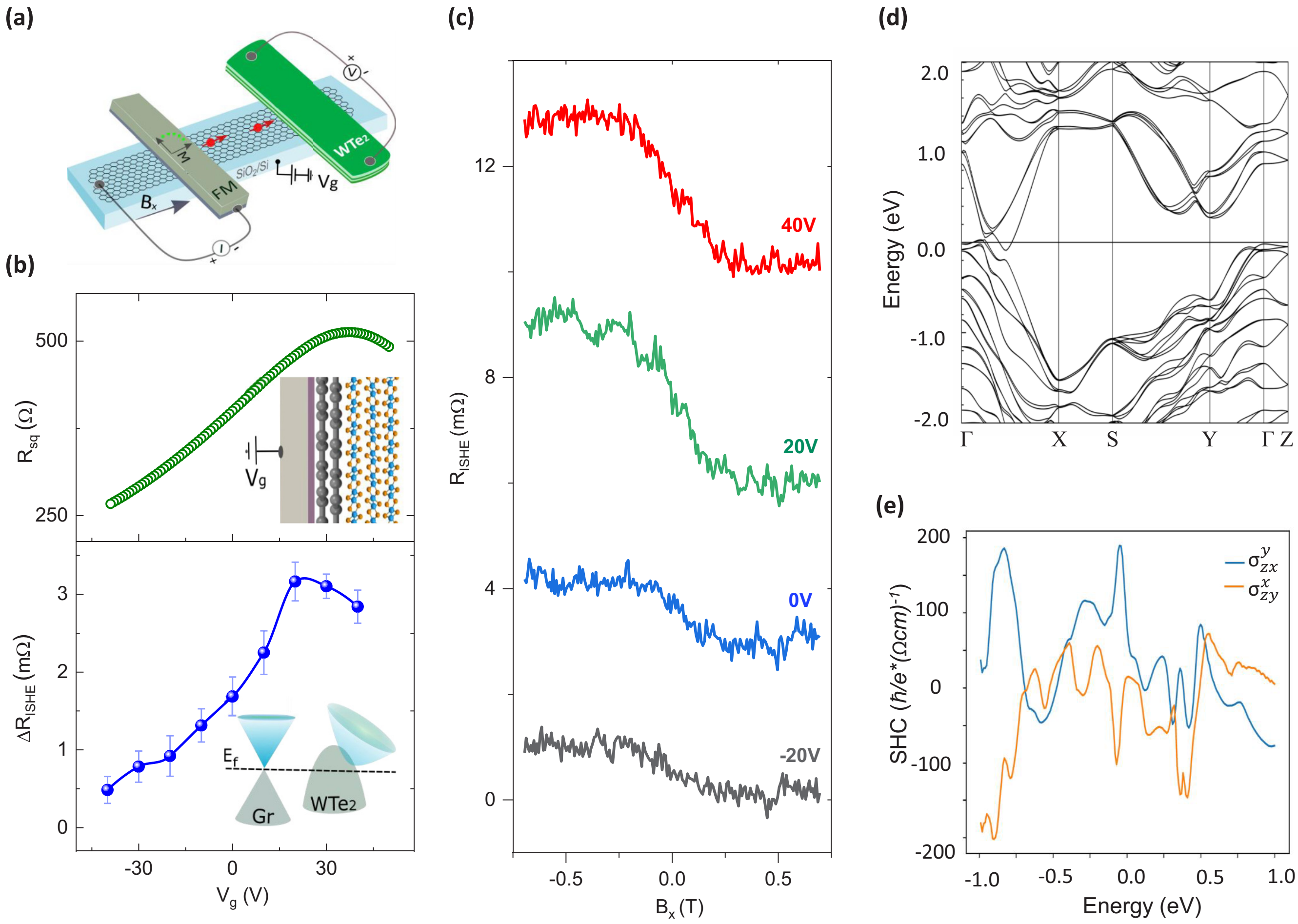

FIG. 4. Gate control of the inverse spin Hall signal in the heterostructure. (a) The ISHE geometry for the gate-voltage-dependent measurements. (b) Top panel: The Dirac curve of the few-layer graphene in the heterostructure channel measured in a local four-terminal measurement geometry. Bottom panel: Gate dependence of the ΔR_{ISHE} signal magnitude for device No. 2 measured in the range of $V_g = -40$ to 40 V at room temperature. The line is a guide to the eye. The insets are the schematic and band structure of a graphene-WTe$_2$ heterostructure with an applied gate voltage (V_g). (c) The measured ISHE resistance R_{ISHE} at different gate voltages with a shift at the y axis for the sake of clarity. (d) Calculated band structure of bulk WTe$_2$ in the T_d phase with the Fermi energy is set to zero. (e) Calculated SHE conductivity, σ^y_{zx} and σ^x_{zy}, with respect to the Fermi energy position in WTe$_2$. All the measurements were performed at 300 K.

precondition to observe the ISHE [42,43] (see details in Note 1 in the Supplemental Material [36]).

The angle-dependent measurements of the ISHE signal [37] were performed in device No. 2 to verify the relation between the direction of the injected spins and the induced charge accumulation in WTe$_2$. The measurements were carried out at a different in-plane B field along the tilting angle φ with respect to the x axis [Fig. 3(a)]. As shown in Fig. 3(b), the measured R_{ISHE} decreases with the transverse magnetic (x-direction) component and vanishes when the magnetization is aligned with the y axis. The sign change of R_{ISHE} is observed between $\varphi = 0^\circ$ and 180° (π) due to switching of the Co magnetization direction and associated reversal of polarization of the spin current. A null R_{ISHE} signal is observed for $\varphi = 90^\circ$ ($\pi/2$) when the magnetization Co is aligned with the y axis, as the injected spins are parallel to the WTe$_2$ long axis and no ISHE voltage is generated in the measured geometry of the WTe$_2$ electrode. The magnitude of the measured ISHE signals ΔR_{ISHE} as a function of the measurement angle φ is shown in Fig. 3(c). As expected, the charge current I_C is proportional to $s \times I_s$ (s is the spin and I_s is the spin current), the angular dependence of the ΔR_{ISHE} is expected to vary with $\cos(\varphi)$. Such angle-dependent behaviors essentially show the characteristics of the ISHE signal [44]. Figures 3(d) and 3(e) show the ISHE signal measured at different spin injection currents, and as expected ΔV_{ISHE} shows a linear behavior with the bias current magnitude. Combined with the bias current polarity dependence (see Fig. S5 in the Supplemental Material [36]), we can rule out all the thermal-related effects [45,46].

The gate dependence of the ISHE measurement was performed in a WTe$_2$-graphene heterostructure (device No. 2) by using the Si/SiO$_2$ as a back gate [Fig. 4(a)]. The gate voltage dependence of the graphene channel resistance across the heterostructure shows the Dirac point at $V_{\mathrm{D}} = 35$ V [Fig. 4(b)], while the WTe$_2$ channel resistance does not show much of a change due to its semimetallic character [Fig. S3(e)]. The gate dependence of the graphene-WTe$_2$ interface resistance shows some modulation due to the change in the graphene Fermi energy [Fig. S3(d)], which may affect the spin absorption efficiency. Figures 4(b) and 4(c) show the magnitude of the ISHE signal ΔR_{ISHE} at different gate voltages. Interestingly, we observe a strong increase of the signal magnitude that reaches a maximum as the gate approaches the graphene Dirac point at $V_g = 30$ V. This contrasts with the weak gate dependence of the spin transport signal across the heterostructure (see Fig. S8 in the Supplemental Material [36]). The gate dependence of the spin transport signal (spin valve and Hanle) is known to be strongly dependent on the ferromagnetic tunnel contact resistances [47]. However, in our case, the nonlocal spin transport signal is almost independent of the gate voltage, while the ISHE signals show a strong modulation. This behavior can be explained by considering the spin detector, i.e., $\mathrm{WTe_2}$-graphene heterostructure instead of the graphene-ferromagnet impedance mismatch [47]. Part of the enhancement in ΔR_{ISHE} can be due to increased spin absorption by $\mathrm{WTe_2}$, i.e., an increase in effective spin current injected vertically at the graphene-$\mathrm{WTe_2}$ interface when the graphene resistance increases near the Dirac point [3,4] or (and) the increase of ISHE efficiency with an electric field.

III. DISCUSSION

The SHE signals observed in our experiment can be rationalized by the conventional bulk SHE and the REE in $\mathrm{WTe_2}$. In an ideal type-I Weyl semimetal (or an ideal topological insulator), in which the bulk Fermi surface vanishes, the bulk SHE is purely contributed by the topological effect [48]. The bulk-induced spin accumulation on the Fermi surface is equivalent to that of the Edelstein effect on the topological Fermi arcs, because of the principle of the bulk-boundary correspondence [49]. However, in a type-II Weyl semimetal, the bulk Fermi states always coexist with the Fermi arcs at the Fermi surface. Therefore, we should consider the SHE to include both Fermi surface state and the bulk state effects. Thus, we perform *ab initio* density-functional theory (DFT) calculations [48,50] to evaluate the SHE in $\mathrm{WTe_2}$. Based on highly symmetric Wannier functions, we construct a tight-binding-type Hamiltonian that can fully reproduce the DFT results. Using the material-specific effective Hamiltonian, we employed the Kubo formula approach [48] to calculate the SHE conductivity. The calculated electronic band structure and SHE conductivity for $\mathrm{WTe_2}$ are shown in Figs. 4(d) and 4(e). Here, we consider the SHE that can be quantitatively estimated from the spin Berry curvature of the band structure. The SHE refers to the generation of a spin current $\boldsymbol{J}_j^i = \boldsymbol{\sigma}_{jk}^i \boldsymbol{E}_k$ induced by an electric field $\boldsymbol{E}_k$, where $i, j, k = x, y, z$ (the crystallographic axes of $\mathrm{WTe_2}$), and $\boldsymbol{J}_j^i$ represents a spin current along the j direction with a spin polarization along i. The SHE conductivity $\boldsymbol{\sigma}_{jk}^i$ characterizes the strength of the SHE. For a charge current along the *ab* plane and spin current along the *c* axis, we obtain the corresponding in-plane SHE conductivities in the range of $\sigma_{\mathrm{SH}} = 14{-}96(\hbar/e)(\Omega\,\mathrm{cm})^{-1}$ due to the large crystal anisotropy. Taking the electronic conductivity of $\mathrm{WTe_2}$ from our measurement, we estimate the theoretical maximum SHE to be with a spin Hall angle of $\theta_{\mathrm{SH}} = \frac{\sigma_{\mathrm{SH}}}{\sigma_{xx}} = 17\%$. The calculated large θ_{SHE} can qualitatively account for the observation of the large SHE signals in our experiments. This is also confirmed by a recent theoretical paper [51], which suggests a large spin Hall angle in $\mathrm{WTe_2}$. Furthermore, as shown in Fig. 4(e), the calculated SHE conductivity is also found to be very sensitive and depends on the position of the Fermi energy in $\mathrm{WTe_2}$. The calculated σ_{SHE} can be considerably tuned by a small change in energy, such as a tiny change in energy at 100 meV below the Fermi energy that can cause a change of σ_{SHE} by nearly an order of magnitude. However, experimentally we could not tune the surface states of $\mathrm{WTe_2}$ to the Fermi level by the application of gate voltage [21,24].

To be noted, one cannot extract a spin Hall angle θ_{SH} and spin diffusion length $\lambda_{\mathrm{WTe_2}}$ at the same time by fitting the out-of-plane (I)SHE signal [40] or solving the in-plane case equation [42] due to the entanglement of the two parameters. Therefore, we take $\theta_{\mathrm{SH}} = 0.013$ from the literature with a comparable $\mathrm{WTe_2}$ thickness [27]. Consequently, the data fitting results in a spin diffusion length of $\lambda_{\mathrm{WTe_2}} = 8 \pm 0.9$ nm. To verify the result, a numerical solution to the in-plane ISHE signal was also obtained. Substituting $\lambda_{\mathrm{WTe_2}}$ into the plot of θ_{SH}-$\lambda_{\mathrm{WTe_2}}$, we find the $\theta_{\mathrm{SH}} = 0.014$, which is consistent with the literature (see details in Note 2 in the Supplemental Material [36]). For the estimation of these spin parameters, we used device No. 3 with monolayer graphene and a narrow and thin $\mathrm{WTe_2}$ flake (width $=1$ μm and thickness $=$ 11 nm) having a very low $\mathrm{WTe_2}$-graphene interface resistance ~ 25 Ω $\mu\mathrm{m}^2$, which is suitable for the use of the 1D model calculation (shown in Table 1 in the Supplemental Material [36]). In contrast, for thicker $\mathrm{WTe_2}$ flakes, the $\mathrm{WTe_2}$-graphene interface resistance is usually hundreds of Ω due to their poor van der Waals adhesion. Therefore, an experimental quantification of the SHE parameters in $\mathrm{WTe_2}$ by the conventional spin absorption method [42,43] is not possible for devices No. 1 and No. 2. Our DFT calculation shows that the bulk and surface states coexist on the Fermi surface of $\mathrm{WTe_2}$, which suggests that both SHE and REE may contribute to the measured spin signal. As SHE is a bulk effect, the thickness dependence of the spin signals is obviously expected, whereas no thickness dependence is expected for REE as the latter is a surface phenomenon. A recent experiment using spin-orbit torque and switching measurements [52] shows the thickness dependence of the charge-spin conversion in $\mathrm{WTe_2}$, which suggests the dominated SHE in the observed signal. Therefore, we expect that the SHE in $\mathrm{WTe_2}$ is most likely dominant in our measurements. Moreover, no sign changes in the ISHE signal near the charge neutrality point [56,59] and a highly suppressed shunting effect between $\mathrm{WTe_2}$ and graphene (see details in Note 2 in the Supplemental Material [36]) rule out the dominance of the proximity-induced effects in graphene in our data, such as proximity-induced REE and proximity-induced SHE.

IV. CONCLUSION

The emergent Weyl semimetal $\mathrm{WTe_2}$ is shown here to be a promising material for charge-spin conversion at room temperature due to its unique electronic band structure giving rise to huge spin-orbit coupling and spin-polarized bulk and surface states. Particularly, the strong spin Hall signal in the $\mathrm{WTe_2}$ devices and the gate tunability of the spin signal provide another tool for potential applications in future spintronic device architectures. Furthermore, as predicted in theoretical calculations, the spin Hall conductivity can be controlled by using Weyl semimetals with a tunable Fermi level [10] and alloys with tunable resistivity [41,53]. This will allow one to achieve systematic control over the charge-spin conversion via electrical and optical means and a better understanding of the Weyl physics. Such measures providing large charge-spin conversion efficiency in Weyl semimetals at room temperature can be used to switch or oscillate the magnetization of nanomagnets with a very low current density. These developments will have a huge potential for emergent spin-orbit-induced phenomena and applications in ultralow-power magnetic random-access memory and spin logic circuits [29,55].

Note added in proof. Recently, we became aware of several reports on charge-spin conversion in semiconductor and semimetal TMDs and their heterostructures with graphene. In these papers, the use of different measurement geometries and interface resistance conditions with graphene provided the observation of a range of charge-spin conversion and proximity-induced phenomena, which we discuss below. In the MoS_2 [5], TaS_2 [54], WS_2 [56], $MoTe_2$ [57], and a topological insulator [58,59], the proximity-induced REE in graphene is proposed to explain the gate-controlled sign change of the signal. Notably, as in most of the cases, the electrical contacts are made on graphene instead of the TMDs, and proximity-induced REE in graphene is generally observed. In addition to SOI-induced effects, the magnetic proximity effect has also been reported using a graphene/Cr_2Ge_2Te heterostructure [60]. In the present paper, by explicitly making contacts to WTe_2, we could measure the SHE in WTe_2 and do not observe any contribution from the proximity-induced REE effect in graphene. Similarly, SHE has also been recently reported in $MoTe_2$ [57] with additional contributions due to the lower-crystal symmetry of the crystal. Recently, using a vertical charge current through a WTe_2/graphene junction with a larger interface resistance [61], our measurements show an out-of-plane electrical-field-induced spin polarization in WTe_2 and subsequent spin injection into the graphene channel at room temperature. Contrary to the conventional SHE presented in the current paper with s, J_s, and J_c being perpendicular to each other, the measured spin injection current shows spin-momentum-locking (SML) characteristics with J_s to be parallel to J_c [61]. The observation of such effects can be possible in the Weyl semimetal WTe_2 due to its lower crystal symmetry or from SML in spin-polarized bulk Fermi states.

ACKNOWLEDGMENTS

The authors at Chalmers University of Technology, Sweden acknowledge financial support from EU FlagEra project (from Swedish Research Council VR No. 2015-06813), Swedish Research Council VR project grant (No. 2016-03658), EU Graphene Flagship (No. 604391), and Graphene Center and the AoA Nano program at Chalmers University of Technology. The authors from University of Science and Technology Beijing, Beijing, China, acknowledge financial support from the National Basic Research Program of China (Grant No. 2015CB921502) and the National Natural Science Foundation of China (Grants No. 51731003 and No. 51471029). B.Z. is thankful for the financial support from the program of China Scholarships Council (File No. 201706460036). We thank our colleagues at the Quantum Device Physics Laboratory and Nanofabrication Laboratory at Chalmers University of Technology for their support.

S.P.D. and B.Z. conceived the idea and designed the experiments. B.Z., D.K., B.K., and S.P.D. fabricated and measured the devices at Chalmers University of Technology. B.Z. and S.P.D. analyzed, interpreted the experimental data, compiled the figures, and wrote the manuscript. D.K., B.K., A.H.M., B.Y., X.X., and Y.J. discussed the results and provided feedback on the manuscript. Y.Z., H.F., and B.Y. performed theoretical calculations on the band structure and SHE conductivity. S.P.D. supervised the project. The authors declare no competing financial interests.

[1] K. S. Novoselov, A. Mishchenko, A. Carvalho, and A. H. Castro Neto, Science **353**, aac9439 (2016).

[2] S. Manzeli, D. Ovchinnikov, D. Pasquier, O. V. Yazyev, and A. Kis, Nat. Rev. Mater. **2**, 17033 (2017).

[3] A. Dankert and S. P. Dash, Nat. Commun. **8**, 16093 (2017).

[4] W. Yan, O. Txoperena, R. Llopis, H. Dery, L. E. Hueso, and F. Casanova, Nat. Commun. **7**, 13372 (2016).

[5] C. K. Safeer, J. Ingla-Aynés, F. Herling, J. H. Garcia, M. Vila, N. Ontoso, M. R. Calvo, S. Roche, L. E. Hueso, and F. Casanova, Nano. Lett. **19**, 1074 (2019).

[6] M. Offidani, M. Milletarì, R. Raimondi, and A. Ferreira, Phys. Rev. Lett. **119**, 196801 (2017).

[7] Q. H. Wang, K. Kalantar-Zadeh, A. Kis, J. N. Coleman, and M. S. Strano, Nat. Nanotechnol. **7**, 699 (2012).

[8] A. Burkov, Nat. Mater. **15**, 1145 (2016).

[9] S. Wu, V. Fatemi, Q. D. Gibson, K. Watanabe, T. Taniguchi, R. J. Cava, and P. Jarillo-Herrero, Science **359**, 76 (2018).

[10] N. P. Armitage, E. J. Mele, and A. Vishwanath, Rev. Mod. Phys. **90**, 15001 (2018).

[11] H. Zheng and M. Zahid Hasan, Adv. Phys. X. **3**, 1466661 (2018).

[12] B. Yan and C. Felser, Annu. Rev. Condens. Matter. Phys. **8**, 337 (2017).

[13] M. N. Ali, J. Xiong, S. Flynn, J. Tao, Q. D. Gibson, L. M. Schoop, T. Liang, N. Haldolaarachchige, M. Hirschberger, N. P. Ong, and R. J. Cava, Nature (London) **514**, 205 (2014).

[14] C. Shekhar, A. K. Nayak, Y. Sun, M. Schmidt, M. Nicklas, I. Leermakers, U. Zeitler, Y. Skourski, J. Wosnitza, Z. Liu, Y. Chen, W. Schnelle, H. Borrmann, Y. Grin, C. Felser, and B. Yan, Nat. Phys. **11**, 645 (2015).

[15] J. Xiong, S. K. Kushwaha, T. Liang, J. W. Krizan, M. Hirschberger, W. Wang, R. J. Cava, and N. P. Ong, Science **350**, 413 (2015).

[16] Y. Zhang, J. van den Brink, C. Felser, and B. Yan, 2D Mater. **5**, 044001 (2018).

[17] B. Q. Lv, S. Muff, T. Qian, Z. D. Song, S. M. Nie, N. Xu, P. Richard, C. E. Matt, N. C. Plumb, L. X. Zhao, G. F. Chen, Z.

Fang, X. Dai, J. H. Dil, J. Mesot, M. Shi, H. M. Weng, and H. Ding, Phys. Rev. Lett. **115**, 217601 (2015).
[18] A. Johansson, J. Henk, and I. Mertig, Phys. Rev. B **97**, 085417 (2018).
[19] Y. Sun, S.-C. Wu, and B. Yan, Phys. Rev. B **92**, 115428 (2015).
[20] A. N. Berger, E. Andrade, A. Kerelsky, D. Edelberg, J. Li, Z. Wang, L. Zhang, J. Kim, N. Zaki, J. Avila, C. Chen, M. C. Asensio, S.-W. Cheong, B. A. Bernevig, and A. N. Pasupathy, npj Quantum Mater. **3**, 2 (2018).
[21] F. Y. Bruno, A. Tamai, Q. S. Wu, I. Cucchi, C. Barreteau, A. de la Torre, S. M. Walker, S. Riccò, Z. Wang, T. K. Kim, M. Hoesch, M. Shi, N. C. Plumb, E. Giannini, A. A. Soluyanov, and F. Baumberger, Phys. Rev. B **94**, 121112 (2016).
[22] P. Li, Y. Wen, X. He, Q. Zhang, C. Xia, Z.-M. Yu, S. A. Yang, Z. Zhu, H. N. Alshareef, and X.-X. Zhang, Nat. Commun. **8**, 2150 (2017).
[23] Y. Wu, D. Mou, N. H. Jo, K. Sun, L. Huang, S. L. Bud'ko, P. C. Canfield, and A. Kaminski, Phys. Rev. B **94**, 121113 (2016).
[24] C. Wang, Y. Zhang, J. Huang, S. Nie, G. Liu, A. Liang, Y. Zhang, B. Shen, J. Liu, C. Hu, Y. Ding, D. Liu, Y. Hu, S. He, L. Zhao, L. Yu, J. Hu, J. Wei, Z. Mao, Y. Shi, X. Jia, F. Zhang, S. Zhang, F. Yang, Z. Wang, Q. Peng, H. Weng, X. Dai, Z. Fang, Z. Xu, C. Chen, and X. J. Zhou, Phys. Rev. B **94**, 241119 (2016).
[25] J. Jiang, F. Tang, X. C. Pan, H. M. Liu, X. H. Niu, Y. X. Wang, D. F. Xu, H. F. Yang, B. P. Xie, F. Q. Song, P. Dudin, T. K. Kim, M. Hoesch, P. K. Das, I. Vobornik, X. G. Wan, and D. L. Feng, Phys. Rev. Lett. **115**, 166601 (2015).
[26] Q. Wang, J. Li, J. Besbas, C.-H. Hsu, K. Cai, L. Yang, S. Cheng, Y. Wu, W. Zhang, K. Wang, T.-R. Chang, H. Lin, H. Chang, and H. Yang, Adv. Sci. **5**, 1700912 (2018).
[27] D. MacNeill, G. M. Stiehl, M. H. D. Guimaraes, R. A. Buhrman, J. Park, and D. C. Ralph, Nat. Phys. **13**, 300 (2017).
[28] P. Li, W. Wu, Y. Wen, C. Zhang, J. Zhang, S. Zhang, Z. Yu, S. A. Yang, A. Manchon, and X. Zhang, Nat. Commun. **9**, 3990 (2018).
[29] K. Garello, F. Yasin, S. Couet, L. Souriau, J. Swerts, S. Rao, S. Van Beek, W. Kim, E. Liu, S. Kundu, D. Tsvetanova, K. Croes, N. Jossart, E. Grimaldi, M. Baumgartner, D. Crotti, A. Fumemont, P. Gambardella, and G. S. Kar, in *Proceedings of the 2018 IEEE Symposium on VLSI Circuits, Honolulu, HI* (IEEE, Piscataway, NJ, 2018), pp. 81–82.
[30] B. Feng, Y.-H. Chan, Y. Feng, R.-Y. Liu, M.-Y. Chou, K. Kuroda, K. Yaji, A. Harasawa, P. Moras, A. Barinov, W. Malaeb, C. Bareille, T. Kondo, S. Shin, F. Komori, T.-C. Chiang, Y. Shi, and I. Matsuda, Phys. Rev. B **94**, 195134 (2016).
[31] M. V. Kamalakar, C. Groenveld, A. Dankert, and S. P. Dash, Nat. Commun. **6**, 6766 (2015).
[32] D. Khokhriakov, B. Karpiak, A. M. Hoque, and S. P. Dash, Carbon, doi: 10.1016/j.carbon.2020.01.103.
[33] S.-Y. Xu, I. Belopolski, D. S. Sanchez, M. Neupane, G. Chang, K. Yaji, Z. Yuan, C. Zhang, K. Kuroda, G. Bian, C. Guo, H. Lu, T.-R. Chang, N. Alidoust, H. Zheng, C.-C. Lee, S.-M. Huang, C.-H. Hsu, H.-T. Jeng, A. Bansil, T. Neupert, F. Komori, T. Kondo, S. Shin, H. Lin, S. Jia, and M. Z. Hasan, Phys. Rev. Lett. **116**, 096801 (2016).
[34] J. Sinova, S. O. Valenzuela, J. Wunderlich, C. H. Back, and T. Jungwirth, Rev. Mod. Phys. **87**, 1213 (2015).
[35] K. Ando E. Saitoh, Nat. Commun. **3**, 629 (2012).
[36] See Supplemental Material at http://link.aps.org/supplemental/10.1103/PhysRevResearch.2.013286 for details about the measurements.
[37] T. Kimura, Y. Otani, T. Sato, S. Takahashi, and S. Maekawa, Phys. Rev. Lett. **98**, 156601 (2007).
[38] L. Onsager, Phys. Rev. **37**, 405 (1931).
[39] S. O. Valenzuela and M. Tinkham, Nature (London) **442**, 176 (2006).
[40] W. Savero Torres, J. F. Sierra, L. A. Benítez, F. Bonell, M. V Costache, and S. O. Valenzuela, 2D Mater. **4**, 041008 (2017).
[41] E. Sagasta, Y. Omori, M. Isasa, M. Gradhand, L. E. Hueso, Y. Niimi, Y. Otani, and F. Casanova, Phys. Rev. B **94**, 060412 (2016).
[42] W. Yan, E. Sagasta, M. Ribeiro, Y. Niimi, L. E. Hueso, and F. Casanova, Nat. Commun. **8**, 661 (2017).
[43] Y. Niimi, M. Morota, D. H. Wei, C. Deranlot, M. Basletic, A. Hamzic, A. Fert, and Y. Otani, Phys. Rev. Lett. **106**, 126601 (2011).
[44] K. Fujiwara, Y. Fukuma, J. Matsuno, H. Idzuchi, Y. Niimi, Y. Otani, and H. Takagi, Nat. Commun. **4**, 2893 (2013).
[45] A. Slachter, F. L. Bakker, J.-P. Adam, and B. J. van Wees, Nat. Phys. **6**, 879 (2010).
[46] J. F. Sierra, I. Neumann, J. Cuppens, B. Raes, M. V. Costache, and S. O. Valenzuela, Nat. Nanotechnol. **13**, 107 (2018).
[47] W. Han, K. Pi, K. M. Mccreary, Y. Li, J. J. I. Wong, A. G. Swartz, and R. K. Kawakami, Phys. Rev. Lett. **105**, 167202 (2010).
[48] Y. Sun, Y. Zhang, C. Felser, and B. Yan, Phys. Rev. Lett. **117**, 146403 (2016).
[49] A. M. Essin and V. Gurarie, Phys. Rev. B **84**, 125132 (2011).
[50] K. Koepernik and H. Eschrig, Phys. Rev. B **59**, 1743 (1999).
[51] J. Zhou, J. Qiao, A. Bournel, and W. Zhao, Phys. Rev. B **99**, 060408 (2019).
[52] S. Shi, S. Liang, Z. Zhu, K. Cai, S. D. Pollard, Y. Wang, J. Wang, Q. Wang, P. He, J. Yu, G. Eda, G. Liang, and H. Yang, Nat. Nanotechnol. **14**, 945 (2019).
[53] T.-R. Chang, S.-Y. Xu, G. Chang, C.-C. Lee, S.-M. Huang, B. Wang, G. Bian, H. Zheng, D. S. Sanchez, I. Belopolski, N. Alidoust, M. Neupane, A. Bansil, H.-T. Jeng, H. Lin, and M. Zahid Hasan, Nat. Commun. **7**, 10639 (2016).
[54] L. Li, J. Zhang, G. Myeong, W. Shin, H. Lim, B. Kim, S. Kim, T. Jin, B. Kim, C. Kim, J. Lischner, A. Ferreira, and S. Cho, arXiv:1906.10702.
[55] A. Soumyanarayanan, N. Reyren, A. Fert, and C. Panagopoulos, Nature (London) **539**, 509 (2016).
[56] T. S. Ghiasi, A. A. Kaverzin, P. J. Blah, and B. J. van Wees, Nano. Lett. **19**, 5959 (2019).
[57] A. M. Hoque, D. Khokhriakov, B. Karpiak, and S. P. Dash, arXiv:1908.09367.
[58] D. Khokhriakov, A. W. Cummings, K. Song, M. Vila, B. Karpiak, A. Dankert, S. Roche, and S. P. Dash, Sci. Adv. **4**, eaat9349 (2018).
[59] D. Khokhriakov, A. M. Hoque, B. Karpiak, and S. P. Dash, arXiv:1910.06760.
[60] B. Karpiak, A. W. Cummings, K. Zollner, M. Vila, D. Khokhriakov, M. A. M. Hoque, A. Dankert, P. Svedlindh, J. Fabian, S. Roche, and S. P. Dash, 2D Mater. **7**, 015026 (2019).
[61] B. Zhao, B. Karpiak, D. Khokhriakov, A. M. Hoque, X. Xu, Y. Jiang, and S. P. Dash, arXiv:1910.06225.